

Resonantly enhanced nonreciprocal silicon Brillouin amplifier

Nils T. Otterstrom,^{1,*} Eric A. Kittlaus,¹ Shai Gertler,¹ Ryan O. Behunin,² Anthony L. Lentine,³ and Peter T. Rakich^{1,†}

¹*Department of Applied Physics, Yale University, New Haven, CT 06520 USA.*

²*Department of Physics and Astronomy, Northern Arizona University, Flagstaff, AZ 86001 USA.*

³*Applied Photonic Microsystems, Sandia National Laboratories, Albuquerque, New Mexico 87185, USA*

(Dated: March 12, 2019)

The ability to amplify light within silicon waveguides is central to the development of high-performance silicon photonic device technologies. To this end, the large optical nonlinearities made possible through stimulated Brillouin scattering offer a promising avenue for power-efficient all-silicon amplifiers, with recent demonstrations producing several dB of net amplification. However, scaling the degree of amplification to technologically compelling levels (> 10 dB), necessary for everything from filtering to small signal detection, remains an important goal. Here, we significantly enhance the Brillouin amplification process by harnessing an inter-modal Brillouin interaction within a multi-spatial-mode silicon racetrack resonator. Using this approach, we demonstrate more than 20 dB of net Brillouin amplification in silicon, advancing state-of-the-art performance by a factor of 30. This degree of amplification is achieved with modest (~ 15 mW) continuous-wave pump powers and produces low out-of-band noise. Moreover, we show that this same system behaves as a unidirectional amplifier, providing more than 28 dB of optical nonreciprocity without insertion loss in an all-silicon platform. Building on these results, this device concept opens the door to new types of all-silicon injection-locked Brillouin lasers, high-performance photonic filters, and waveguide-compatible distributed optomechanical phenomena.

I. INTRODUCTION

High-performance optical amplification is an essential functionality in integrated photonic circuits. Within the context of silicon photonics, however, strategies for robust integrated amplifiers have faced significant challenges that stem from silicon's indirect bandgap and high levels of nonlinear loss [1, 2]. To date, silicon amplifier technologies have relied on either hybrid integration strategies [3–6] or nonlinear optical interactions [1] such as Raman [7–10] or Kerr effects [11–13]. While Raman and Kerr interactions have been used to produce net amplification using pulsed optical pumping [7–11], active electrical removal of free carriers [14], or large mid-IR pump powers [12, 13], it remains nontrivial to achieve large degrees of power-efficient optical amplification due to the competition between gain and nonlinear absorption in silicon.

Recently, nonlinear light-sound coupling known as stimulated Brillouin scattering has emerged as a promising mechanism for optical amplification in silicon, with dynamics and performance that can be customized through structural control [15, 16]. Once entirely absent from silicon photonics, these Brillouin interactions have emerged as one of the strongest and most tailorable nonlinearities in silicon [16, 17], opening the door to net optical amplification [18–20] and Brillouin lasing in silicon photonic circuits [21]. While recent demonstrations have achieved 2–5 dB of amplification [19, 20], scaling the degree of amplification to levels necessary for high-fidelity filtering [22–25] and small-signal detection schemes [26] remains a nontrivial challenge [27].

In this letter, we demonstrate record-high Brillouin gain and amplification in a silicon waveguide through a resonantly enhanced Brillouin interaction. This all-silicon amplifier system is based on a stimulated inter-modal Brillouin scattering process, in which a traveling elastic wave mediates nonlinear energy transfer between light waves propagating in distinct optical spatial modes [20]. Building on existing device concepts for silicon Brillouin lasers [21], we harness and dramatically enhance this stimulated Brillouin process using a multi-spatial-mode racetrack resonator system that is interfaced with mode-specific couplers to allow signal light to be amplified as it is transmitted through the system. We use this device to realize 30 dB of Brillouin gain, corresponding to over 20 dB of net Brillouin amplification. These results represent a > 30 -fold improvement beyond state-of-the-art Brillouin amplification in silicon [19]. Leveraging the unidirectional amplification produced by this phase-matched process, we also use this system to demonstrate more than 28 dB of nonreciprocal contrast between forward- and backward-propagating waves. This scheme provides robust optical nonreciprocity without insertion loss. Beyond the results presented here, this device concept opens the door to chip-integrated injection-locked Brillouin lasers, microwave-photonic filtering techniques, and distributed optomechanical phenomena.

II. RESULTS

We use a resonant optical configuration to produce greatly enhanced inter-modal Brillouin amplification and optical nonreciprocity in an all-silicon structure. This strategy allows us to transform the otherwise modest amplification (~ 2 dB) possible in a linear geometry (using a waveguide of the same design; see Ref. [20]), into more than 20 dB of net amplification. We achieve this significant enhancement in performance by leveraging the resonator geometry diagrammed in Fig. 1a that builds upon the laser structure described in Ref. [21]. In this type of configuration, resonant transmission through the system becomes lossless (i.e., approaches unity) if the internal gain produced by stimulated inter-modal Brillouin scattering balances the internal losses of the resonator. In

* nils.otterstrom@yale.edu

† peter.rakich@yale.edu

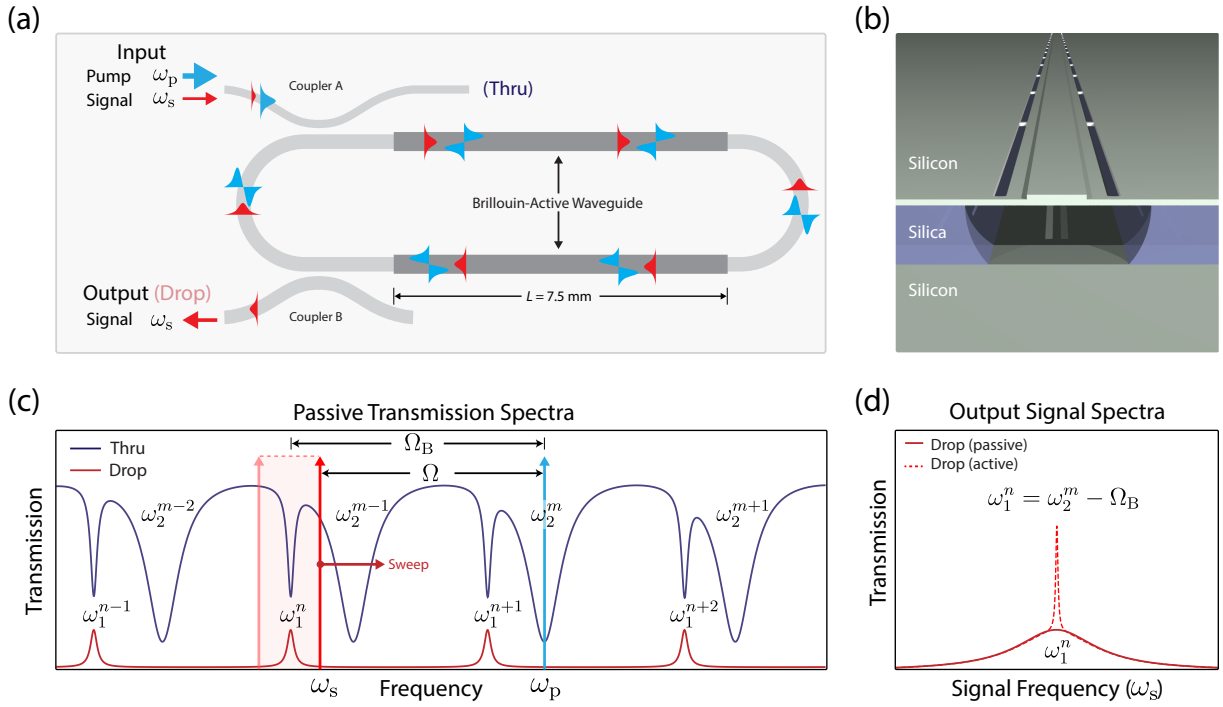


FIG. 1. (a) Resonantly enhanced Brillouin amplifier device concept and operation scheme. The amplifier is composed of a multi-spatial-mode racetrack resonator with two Brillouin-active regions. Using the frequency selectivity of the cavity, pump (ω_p) and signal waves (ω_s) are coupled into the antisymmetric and symmetric cavity modes, respectively, via a multimode coupler. As the pump and signal waves traverse the Brillouin-active segments, the pump wave resonantly amplifies the signal wave through stimulated inter-modal Brillouin scattering. The signal wave exits the system through a mode-selective coupler (drop port), which is designed to couple strongly to the symmetric mode and weakly to the antisymmetric mode. (b) Schematic illustrating the cross-sectional geometry of the Brillouin-active regions. This suspended multimode silicon waveguide supports two transverse electric (TE)-like optical spatial modes and a 6-GHz antisymmetric Lamb-like elastic wave, which mediates inter-modal Brillouin amplification. (c) Idealized optical transmission spectra at the thru and drop ports. Coupling into the racetrack resonator via a multimode coupler yields a characteristic multimode transmission spectrum at the thru port, with broad (centered at ω_2^m) and narrow (centered at ω_1^n) resonances corresponding to the antisymmetric and symmetric optical spatial modes, respectively. The mode-selective drop port is designed to couple out only the symmetric cavity modes. Resonantly-enhanced Brillouin amplification measurements are performed by coupling the pump wave (ω_p) to an antisymmetric cavity mode (ω_2^m) and sweeping the signal wave (ω_s) through a symmetric cavity mode (ω_1^n) that is red-shifted from by the Brillouin frequency (Ω_B). (d) Zoomed-in transmission spectrum for the signal wave exiting the drop port when $\omega_s \approx \omega_1^n$ with (active) and without (passive) the Brillouin gain supplied by the pump wave.

the case when the gain exceeds the internal losses of the resonator, but does not exceed the total loss (i.e., internal + external), the system can yield greater-than-unity transmission without producing self-oscillation (i.e., below the laser threshold). In the limit when the gain approaches the total loss of the system, the degree of amplification can become arbitrarily large—in principle, limited only by gain depletion. Furthermore, we show that due to the phase-matching requirements of the stimulated inter-modal Brillouin process, this resonantly enhanced amplification is unidirectional, yielding large degrees of optical nonreciprocity.

The resonantly enhanced Brillouin amplifier consists of a 15 mm-long racetrack cavity that possesses two Brillouin-active regions (Fig. 1a). The device is fabricated from a single-crystal SOI wafer using a hybrid CMOS-MEMS process (see Appendix C3). The racetrack cavity is formed from a multimode silicon ridge waveguide that supports low-loss guidance of transverse electric (TE)-like symmetric and antisymmetric optical spatial modes. In the Brillouin-active regions, this multimode optical wave-

guide is suspended to provide acoustic guidance for the 6-GHz traveling elastic wave that mediates strong inter-modal Brillouin coupling (see Fig. 1b; for waveguide dimensions, see Appendix C3). Within the resonator, the symmetric and antisymmetric optical spatial modes form two distinct sets of resonances. The symmetric spatial mode produces a set of high-Q factor ($Q_1 = 10^6$) cavity modes centered at frequencies $\{\omega_1^n\}$ while the antisymmetric spatial mode produces a set of cavity modes having lower Q factors ($Q_2 = 2 \times 10^5$) at frequencies $\{\omega_2^m\}$.

To access these cavity modes, the resonator is interfaced with two different directional couplers that permit efficient, mode-specific coupling into and out of the resonator. The input coupler (coupler A) is designed to couple appreciably to both optical spatial modes, producing a characteristic cavity transmission (thru) spectrum with two distinct sets of resonant features (see in Fig. 1c). The broad (narrow) resonances correspond to the cavity modes produced by the antisymmetric (symmetric) optical spatial mode. Using the frequency selectivity of the resonator, the pump light (ω_p) is resonantly coupled into an antisym-

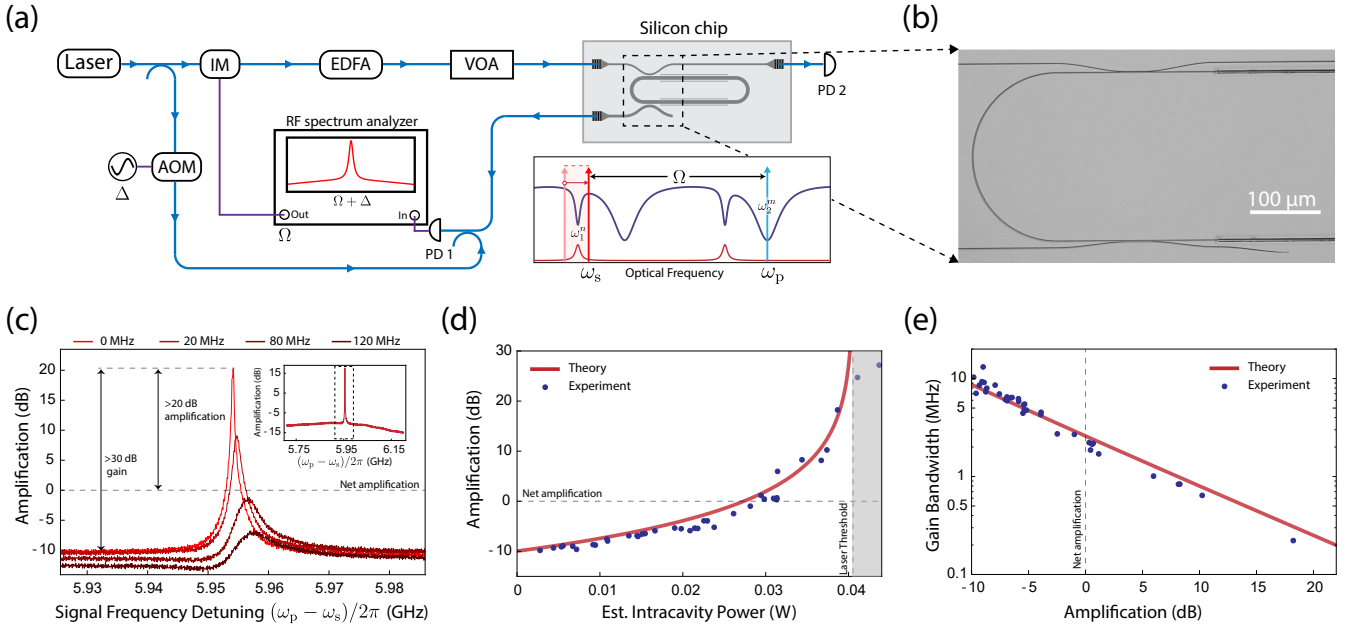


FIG. 2. (a) Diagram of the experimental apparatus used to characterize the resonantly enhanced Brillouin amplifier. Laser light is split along two paths. One path is used to synthesize an optical local oscillator (LO) using an acousto-optic modulator (AOM), which blueshifts the light by $\Delta = 2\pi \times 44$ MHz. The other arm synthesizes pump and signal waves with the desired frequency detuning ($\Omega = \omega_p - \omega_s$) and powers using an intensity modulator (IM), erbium-doped-fiber amplifier (EDFA), and variable optical attenuator (VOA); the light is subsequently coupled on-chip for nonlinear amplification measurements. After passing through the device, the signal wave is coupled through the drop port and off-chip, where it is combined with the blueshifted LO and measured on a high-speed photodetector (PD 1). The RF spectrum analyzer sweeps the detuning (Ω) and measures the microwave power at $(\Omega + \Delta)$, permitting single-sideband measurements of $\omega_s = \omega_p - \Omega$ (without crosstalk from light at $\omega_p + \Omega$). (b) Optical micrograph (in gray scale) showing a top-down view of part of the device. (c) Gain spectra as a function of signal-wave detuning around the Brillouin resonance, showing more than 30 dB of gain and 20 dB of net amplification. Each trace represents a different estimated detuning of the optical cavity mode relative to the Brillouin frequency (see zoomed-out inset). Large optical cavity detunings relative to the Brillouin resonance diminish the degree of amplification and result in characteristic asymmetric line-shapes. (d) Measured and theoretical signal-wave amplification produced over a range of intracavity powers. As the pump power approaches the laser threshold power, the resonantly enhanced Brillouin amplification increases dramatically. Data is compiled from a series of power, microwave-frequency detuning, and wavelength sweeps (for more details see Appendix C2). (e) Linewidth narrowing of the gain bandwidth as a function of signal wave amplification.

metric cavity mode while the signal light (ω_s) is coupled into the symmetric cavity mode. Signal light circulating in the symmetric cavity mode exits the resonator through a mode-selective coupler (coupler B), which preferentially couples to the symmetric spatial mode (see Appendix B for details).

When the pump wave is resonant with an antisymmetric cavity mode ($\omega_p = \omega_2^m$) and a symmetric cavity mode satisfies the Brillouin condition ($\omega_1^n = \omega_2^m - \Omega_B$), signal light injected into the symmetric cavity mode (ω_1^n) can experience resonantly enhanced Brillouin amplification. Through experiments, we couple the pump and signal waves into the antisymmetric and symmetric cavity modes of the racetrack resonator via coupler A. Within the resonator, the co-propagating pump and signal waves nonlinearly couple as they traverse the Brillouin-active regions of the racetrack, producing Brillouin energy transfer and single-sideband gain through stimulated inter-modal Brillouin scattering [20]. As the pump power approaches the threshold for lasing, the degree of amplification is significantly enhanced (see Fig. 1d).

A. Experimental results

We characterize the resonantly enhanced Brillouin amplifier through nonlinear laser spectroscopy measurements using the setup diagrammed in Fig. 2a. All measurements are performed at room temperature and atmospheric pressure using $1.5 \mu\text{m}$ wavelengths. In this experimental scheme, light from a tunable laser is split along two paths; the upper path is used to synthesize the pump and signal waves, while the lower arm is used to create an optical local oscillator (LO) for heterodyne analysis of the emitted signal wave. The optical LO (lower arm) is generated by an acousto-optic modulator, which blueshifts the light by $\Delta = 2\pi \times 44$ MHz. The upper path uses an intensity modulator (IM), erbium-doped fiber amplifier (EDFA), and variable optical attenuator (VOA) to synthesize pump and signal waves of a desired power and variable frequency detuning. Pump and signal waves are then coupled on-chip through a grating coupler; the light is subsequently routed to the racetrack resonator through a single-mode waveguide. Signal light exiting the device is combined with the optical LO and measured using a high-speed photo-receiver for heterodyne spectral analy-

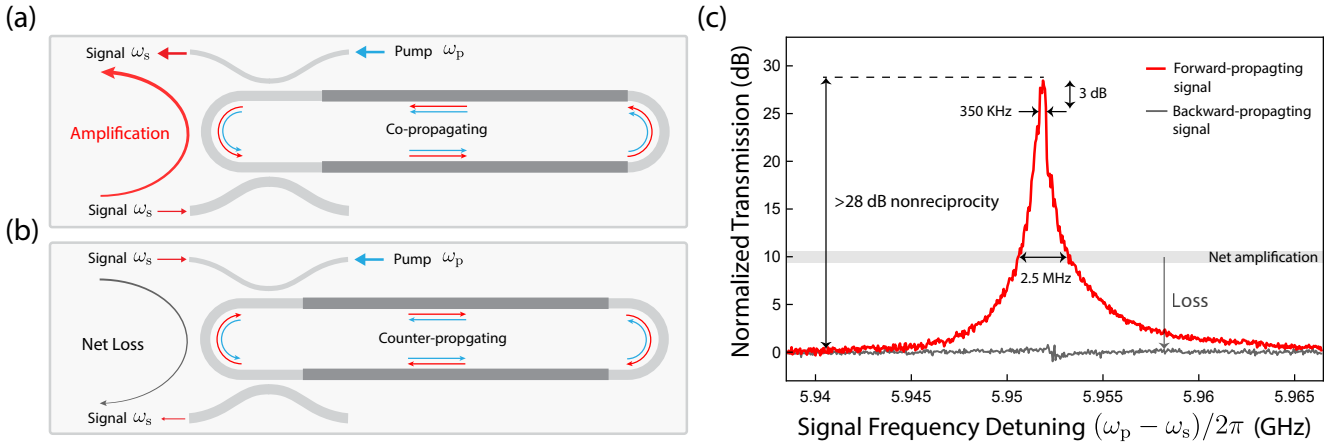


FIG. 3. Demonstration of unidirectional optical amplification and nonreciprocity (For experimental apparatus, see Appendix C1) (a) Experimental arrangement for directional amplification. Pump and signal waves are injected through respective multimode (top) and mode-specific (bottom) couplers such that they co-propagate (forward direction) within the resonator. This configuration allows pump and signal waves to nonlinearly couple through a stimulated forward inter-modal Brillouin process, yielding net amplification of the signal wave. (b) By contrast, a signal wave propagating in the opposite (backward) direction, does not experience Brillouin gain as a result of phase matching; the elastic wave that mediates forward inter-modal scattering is not phase-matched to the backward-scattering process. Thus, in this backward configuration, the signal wave experiences net loss resulting from linear transmission through the resonator. (c) Experimental demonstration of unidirectional amplification. Signal transmission through the system in the forward (red; co-propagating with the pump) and backward (gray; counter-propagating with the pump) directions as a function of signal frequency detuning $\Omega/2\pi$. This system yields a maximum 28 dB of nonreciprocity (with a FWHM of 350 KHz) and provides > 10 dB of isolation over a 2.5 MHz bandwidth.

sis. We sweep a microwave oscillator at Ω to synthesize the signal wave at $\omega_s = \omega_p - \Omega$, and synchronously detect at $\Omega + \Delta$ using a spectrum analyzer. By tracking at this offset frequency (Δ), we are able to selectively detect the redshifted signal wave ($\omega_p - \Omega$) without crosstalk from the blueshifted tone ($\omega_p + \Omega$).

Using this experimental configuration, we sweep the laser wavelength, pump power, and signal-wave detuning to characterize the amplifier system. In the limit of low pump power, no Brillouin gain is produced, and we recover the linear resonant response produced by the symmetric mode of the racetrack cavity. When the pump power is increased, we observe a narrow gain peak at the Brillouin frequency atop the linear resonator response (see Fig. 1d). As the pump power approaches the laser threshold power, we observe a dramatic increase in the degree of resonantly enhanced amplification, consistent with our theoretical predictions (see Fig. 2c-d). Just below threshold, this resonantly enhanced interaction is sufficient to yield in excess of 30 dB of gain, representing more than 20 dB of net amplification after accounting for losses produced by linear transmission through the resonator (see Fig. 2c). The degree of amplification depends strongly on the mode-pair detuning (i.e., the frequency separation $\omega_2^m - \omega_1^n$) relative to the Brillouin frequency, as shown in Fig. 2c. In addition, we observe that the gain bandwidth scales inversely with the amplification as a result of gain narrowing, in agreement with theory (see Fig. 2e).

Owing to the phase-matching characteristics of this inter-band Brillouin process, we show that this system yields unidirectional gain that results in a highly nonreciprocal response. This is because the phonon required for the resonantly enhanced Brillouin process mediates gain between co-propagating pump and signal waves, but

does not produce Brillouin coupling between counter-propagating waves [28, 29]. We demonstrate these dynamics by coupling the pump wave into the anti-symmetric resonator mode with a counter-clockwise orientation; we then examine the reciprocity of the system by injecting the signal wave in the forward (Fig. 3a) and backward (Fig. 3b) directions such that the signal wave co- and counter-propagates with the pump wave within the resonator, respectively. When energy conservation is satisfied ($\omega_p = \omega_s + \Omega_B$), the forward configuration yields net amplification (red) of the signal wave, while the backward configuration yields net loss (gray) as a result of linear transmission through the cavity in the absence of gain. Using a fiber-coupled switch, we alternate between the forward and backward configurations while measuring the transmission as a function of signal-wave detuning. As shown in Fig. 3c, these measurements reveal a peak optical nonreciprocity of 28 dB and a bandwidth of 2.5 MHz over which the system provides > 10 dB of optical isolation with no insertion loss (see Appendix C1 for more details).

B. Theory

To understand our observations, we develop a mean-field analytical model that captures the salient amplification and noise dynamics of this resonantly enhanced amplification process (for detailed derivation, see Appendix A). This model treats the pump, signal, and phonon fields as distinct modes that are nonlinearly coupled through stimulated inter-modal Brillouin scattering. Taking a Fourier transform in time allows us to solve for the output signal power spectrum $|S^{\text{out}}[\omega_s]|^2$ relative to the input

signal power spectrum $|S^{\text{in}}[\omega_s]|^2$, yielding

$$\frac{|S^{\text{out}}[\omega_s]|^2}{|S^{\text{in}}[\omega_s]|^2} = \left| \frac{\sqrt{\gamma_{A,1}}\sqrt{\gamma_{B,1}}}{-i(\omega_s - \omega_1^n) + \frac{\gamma_{\text{tot},1}}{2} - \frac{G_B P v_{g,1} \Gamma/4}{i(\Omega_B + \omega_s - \omega_p) + \Gamma/2}} \right|^2, \quad (1)$$

where $\gamma_{\text{tot},1}$ is the total loss rate for the symmetric spatial mode (defined by $\gamma_{\text{tot},1} \equiv \gamma_{A,1} + \gamma_{B,1} + \alpha_1 v_{g,1}$), $\gamma_{(A,B),1}$ are the dissipation rates for the symmetric spatial mode due to couplers A and B ($\gamma_{(A,B),1} \equiv -(2v_{g,1}/L) \ln(1 - \mu_{(A,B),1}^2)^{1/2}$), $v_{g,1}$ is the group velocity of the symmetric optical spatial mode, $\mu_{(A,B),1}^2$ is the coupling constant of couplers A or B for the symmetric spatial mode, L is the length of the racetrack resonator, P is the intracavity pump power, α_1 is the linear propagation loss of the symmetric spatial mode, G_B is the Brillouin gain coefficient, and Γ is the dissipation rate for the acoustic field.

Equation 1 can be used to self-consistently predict the amplification and gain bandwidth of the system and is the basis for the theoretical trends plotted in Fig. 2d-e. Using this framework, we also analyze the noise dynamics and gain depletion produced in this Brillouin amplifier (for detailed analysis of the noise figure and gain depletion, see Appendix A2-3). We note that Eq. 1 diverges at the laser threshold condition, which is an artifact of the stiff pump approximation in this analysis. While the equations are consistent with those describing parametric amplification in cavity-optomechanical systems [30], we note that this analysis requires a mean-field treatment of a distributed, heavily spatially damped phonon field, which is valid only in the presence of the pump and Stokes field (for further discussion, see Ref. [21]).

III. DISCUSSION

In this paper, we have demonstrated that a resonant optical configuration can be used to dramatically enhance the stimulated inter-modal Brillouin scattering process, yielding record-high Brillouin gain and net amplification in an all-silicon chip-integrated system. These results represent a 500-fold improvement in gain and more than a $60\times$ enhancement in net amplification relative to linear (non-resonant) devices of the same design [20]. Building on this work, even greater degrees of optical amplification may be realized by increasing the passive signal transmission while maintaining a low laser threshold; this may be accomplished through further optimization of the mode-specific coupler design or multimode optomechanical waveguide.

As a byproduct of this resonantly enhanced interaction, we also show that this process yields characteristic narrowing of the gain bandwidth (from 10 MHz to sub-MHz) as the pump power approaches the laser threshold power. While broadband amplification is desirable for many applications, the narrowband amplification produced through this resonantly enhanced system presents its own set of intriguing opportunities. In contrast to broadband amplification, in which spontaneous emission or scattering can produce substantial noise over an equally large bandwidth, the narrowband nature of the interaction yields low out-

of-band noise (for details, see Appendix A2). In addition, the narrow, tailorable nature of the gain bandwidth could prove advantageous for many on-chip functionalities, including narrow-band optical and microwave-photonic filters [22, 23], carrier recovery for microwave photonic signal processing [31], and tunable time delay [30, 32–34].

In addition, the unidirectional nature of this Brillouin amplifier opens the door to new types of all-silicon, chip-integrated nonreciprocal technologies. These nonreciprocal dynamics are closely related to those recently demonstrated in cavity-optomechanical and nonlinear optical systems, where time modulation produced through a parametric coupling can produce directional absorption or amplification [35, 36]. While similar behaviors have been demonstrated in glass micro-resonators [37–41], photonic crystal fibers [28], and in silicon optomechanical crystals at cryogenic temperatures [42], this form of nonreciprocity has not previously been demonstrated in a silicon system at room temperature. Moreover, though narrowband in comparison, the level of nonreciprocity demonstrated here (~ 30 dB) is competitive with that achievable using integrated magneto-optic [43–46] or acousto-optic strategies [47, 48]. While magneto-optic-based silicon-photonic isolator and circulator technologies are advancing steadily, they require complex fabrication techniques [43–46]. Acousto-optic strategies are also very promising; however, they have yet to achieve efficiencies necessary to produce optical isolation with low insertion losses [47, 48]. As such, the optical nonreciprocity we demonstrate here—in an all-silicon device with no insertion loss—represents an important step towards practical isolator and circulator technologies in silicon photonics.

In summary, we have demonstrated record-high Brillouin gain and amplification in an integrated silicon photonic circuit. This device is capable of delivering more than 30 dB of gain and 20 dB of net amplification, representing a 30-fold improvement over state-of-the-art performance [19]. Moreover, we show that this phase-matched stimulated Brillouin process is intrinsically unidirectional, yielding more than 28 dB of nonreciprocal contrast between forward- and backward-propagating waves. These results represent an important milestone for Brillouin-based amplifier and isolator technologies in silicon photonics and open the door to new schemes for high-performance microwave photonic filtering, tunable time delay, and injection-locked Brillouin lasers.

FUNDING INFORMATION

This material is based upon work supported by the Packard Fellowship for Science and Engineering, the National Science Foundation Graduate Research Fellowship under Grant No. DGE1122492 (N.T.O.), and the Laboratory Directed Research and Development program at Sandia National Laboratories. Sandia National Laboratories is a multi-program laboratory managed and operated by National Technology and Engineering Solutions of Sandia, LLC., a wholly owned subsidiary of Honeywell International, Inc., for the U.S. Department of Energy's National Nuclear Security Administration under contract DE-NA-0003525. This paper describes objective techni-

cal results and analysis. Any subjective views or opinions that might be expressed in the paper do not necessarily represent the views of the U.S. Department of Energy, the National Science Foundation, or the United States Gov-

ernment.

ACKNOWLEDGEMENTS

We thank Prashanta Kharel for valuable discussions and for assistance in developing the experimental apparatus.

CONTENTS

I. Introduction	1
II. Results	1
A. Experimental results	3
B. Theory	4
III. Discussion	5
Funding Information	5
Acknowledgements	6
A. Dynamics of resonantly enhanced Brillouin amplifier	8
1. Mean-field analysis	8
2. Noise dynamics	9
a. Experimental measure of noise	11
3. Gain depletion	11
B. Passive resonator properties	12
C. Experimental considerations and data analysis	12
1. Nonreciprocal amplification characterization	12
2. System parameters and data analysis	13
3. Device fabrication	14
References	14

Appendix A: Dynamics of resonantly enhanced Brillouin amplifier

1. Mean-field analysis

In this section, we describe a simple mean-field treatment of the amplifier dynamics that is sufficient to capture the salient behavior of the resonantly enhanced inter-modal Brillouin process. Combining mean-field analysis of the full spatio-temporal dynamics of a resonant Brillouin system (see Supplementary Materials of Ref. [21]) with standard coupled-mode theory [49], we can express the equations of motion as

$$\begin{aligned}\dot{a}_s(t) &= -i\omega_1^n a_s(t) - \frac{\gamma_{\text{tot},1}}{2} a_s(t) - ig^* a_p(t) b^\dagger(t) + \sqrt{\gamma_{A,1}} S^{\text{in}}(t) + \sqrt{\gamma_{A,1}} S_A^{\text{N}}(t) + \sqrt{\gamma_{B,1}} S_B^{\text{N}}(t) + \sqrt{\gamma_{R,1}} S_R^{\text{N}}(t) \\ \dot{b}(t) &= -i\Omega_B b(t) - \frac{\Gamma}{2} b(t) - ig^* a_p(t) a_s^\dagger(t) + \eta(t) \\ \dot{a}_p(t) &= -i\omega_2^m a_p(t) - \frac{\gamma_{\text{tot},2}}{2} a_p(t) - ig a_s(t) b(t) + \sqrt{\gamma_{A,2}} S_p^{\text{in}}(t) + \sqrt{\gamma_{\text{tot},2}} S_{\text{tot},2}^{\text{N}}(t).\end{aligned}\quad (\text{A1})$$

Here, $a_s(t)$, $b(t)$, and $a_p(t)$ are the coupled-mode amplitudes for the signal, phonon, and pump fields, respectively, with units of $[\sqrt{\text{number}}]$; $S^{\text{in}}(t)$ and $S_p^{\text{in}}(t)$ represent the input signal-wave and pump-wave fields (with units $[\sqrt{\text{number} \times \text{Hz}}]$); g is the acousto-optic coupling; $\eta(t)$ is the mechanical stochastic driving term that is consistent with the fluctuation-dissipation theorem, with a two-time correlation function of $\langle \eta^\dagger(t') \eta(t) \rangle = \Gamma(n_{\text{th}} + 1/2) \delta(t - t')$, where n_{th} is the thermal occupation of the phonon field; $S_{(A,B,R)}^{\text{N}}(t)$ represent the vacuum fluctuations associated with the optical losses produced by (A) coupler A, (B) coupler B, and (R) the intrinsic loss of the of the racetrack resonator, each with a two-time correlation function given by $\langle S_{(A,B,R)}^{\text{N}\dagger}(t') S_{(A,B,R)}^{\text{N}}(t) \rangle = (1/2) \delta(t - t')$; $S_{\text{tot},2}^{\text{N}}(t)$ represents the vacuum fluctuations associated with the total loss experienced by an antisymmetric optical spatial mode; $\gamma_{\text{tot},(1,2)}$ is the total loss rate for the symmetric and antisymmetric spatial modes (defined by $\gamma_{\text{tot},(1,2)} \equiv \gamma_{A,(1,2)} + \gamma_{B,(1,2)} + \alpha_{(1,2)} v_{g,(1,2)}$); $\gamma_{(A,B),(1,2)}$ are the dissipation rates for the symmetric and antisymmetric spatial modes due to couplers A and B ($\gamma_{(A,B),(1,2)} \equiv -(2v_{g,(1,2)}/L) \ln(1 - \mu_{(A,B),(1,2)}^2)^{1/2}$) while $\gamma_{R,1}$ represents the internal losses of the racetrack resonator for the symmetric mode ($\gamma_{R,1} = \alpha_1 v_{g,1}$); $v_{g,(1,2)}$ is the group velocity of the symmetric and antisymmetric optical spatial modes; L is the length of the racetrack resonator; $\alpha_{(1,2)}$ is the linear propagation loss of the symmetric and antisymmetric spatial mode; Γ is the dissipation rate for the acoustic field.

Using the rotating-wave approximation, we center each field around DC, yielding

$$\begin{aligned}\dot{\bar{a}}_s(t) &= i(\omega_s - \omega_1^n) \bar{a}_s(t) - \frac{\gamma_{\text{tot},1}}{2} \bar{a}_s(t) - ig^* \bar{a}_p(t) \bar{b}^\dagger(t) + \sqrt{\gamma_{A,1}} \bar{S}^{\text{in}}(t) + \sqrt{\gamma_{A,1}} \bar{S}_A^{\text{N}}(t) + \sqrt{\gamma_{B,1}} \bar{S}_B^{\text{N}}(t) + \sqrt{\gamma_{R,1}} \bar{S}_R^{\text{N}}(t) \\ \dot{\bar{b}}(t) &= i(\Omega - \Omega_B) \bar{b}(t) - \frac{\Gamma}{2} \bar{b}(t) - ig^* \bar{a}_p(t) \bar{a}_s^\dagger(t) + \bar{\eta}(t) \\ \dot{\bar{a}}_p(t) &= i(\omega_p - \omega_2^m) \bar{a}_p(t) - \frac{\gamma_{\text{tot},2}}{2} \bar{a}_p(t) - ig \bar{a}_s(t) \bar{b}(t) + \sqrt{\gamma_{A,2}} \bar{S}_p^{\text{in}}(t) + \sqrt{\gamma_{\text{tot},2}} \bar{S}_{\text{tot},2}^{\text{N}}(t),\end{aligned}\quad (\text{A2})$$

where $a_s(t) = \bar{a}_s(t) \exp(-i\omega_s t)$, $a_p(t) = \bar{a}_p(t) \exp(-i\omega_p t)$, and $b(t) = \bar{b}(t) \exp(-i\Omega t)$; $\bar{\eta}(t)$, $\bar{S}^{\text{in}}(t)$, $\bar{S}_{(A,B,R)}^{\text{N}}(t)$, $\bar{S}_{\text{tot},2}^{\text{N}}(t)$, and $\bar{S}_p^{\text{in}}(t)$ are shifted in like manner. We also note that the above requires $\omega_p = \omega_s + \Omega$, consistent with our experimental scheme.

For simplicity, we treat the pump wave as undepleted (i.e., $\dot{\bar{a}}_p = 0$ and $\bar{a}_p(t) = \bar{a}_p$) and ignore the vacuum fluctuations associated with the pump. We next take a Fourier transform of Eq. A2 in time, yielding

$$\begin{aligned}-i\omega \bar{a}_s[\omega] &= i(\omega_s - \omega_1^n) \bar{a}_s[\omega] - \frac{\gamma_{\text{tot},1}}{2} \bar{a}_s[\omega] - ig^* \bar{a}_p \bar{b}^\dagger[\omega] + \sqrt{\gamma_{A,1}} \bar{S}^{\text{in}}[\omega] + \sqrt{\gamma_{A,1}} \bar{S}_A^{\text{N}}[\omega] + \sqrt{\gamma_{B,1}} \bar{S}_B^{\text{N}}[\omega] + \sqrt{\gamma_{R,1}} \bar{S}_R^{\text{N}}[\omega] \\ -i\omega \bar{b}[\omega] &= i(\Omega - \Omega_B) \bar{b}[\omega] - \frac{\Gamma}{2} \bar{b}[\omega] - ig^* \bar{a}_p \bar{a}_s^\dagger[\omega] + \bar{\eta}[\omega].\end{aligned}\quad (\text{A3})$$

Next, we solve these two coupled equations, yielding

$$\begin{aligned}\bar{a}_s[\omega] &= \frac{1}{-i(\omega + \omega_s - \omega_1^n) + \frac{\gamma_{\text{tot},1}}{2} - \frac{|g|^2 |\bar{a}_p|^2}{-i(\omega + \Omega - \Omega_B) + \frac{\Gamma}{2}}} \left[\sqrt{\gamma_{A,1}} \bar{S}^{\text{in}}[\omega] \right. \\ &\quad \left. + \frac{-ig^* \bar{a}_p \bar{\eta}[\omega]}{-i(\omega + \Omega - \Omega_B) + \frac{\Gamma}{2}} + \sqrt{\gamma_{A,1}} \bar{S}_A^{\text{N}}[\omega] + \sqrt{\gamma_{B,1}} \bar{S}_B^{\text{N}}[\omega] + \sqrt{\gamma_{R,1}} \bar{S}_R^{\text{N}}[\omega] \right].\end{aligned}\quad (\text{A4})$$

We proceed by transforming out of the rotating frame and calculating the output signal spectrum by noting that $S^{\text{out}}[\omega_s, \omega] = \sqrt{\gamma_{B,1}} a_s[\omega_s, \omega] - S_B^{\text{N}}[\omega]$, yielding

$$S^{\text{out}}[\omega_s, \omega] = T[\omega] \left[\sqrt{\gamma_{A,1}} S^{\text{in}}[\omega_s + \omega] + \frac{-ig^* \bar{a}_p \bar{\eta}[\omega]}{-i(\omega + \Omega - \Omega_B) + \frac{\Gamma}{2}} + \sqrt{\gamma_{A,1}} \bar{S}_A^N[\omega] + \sqrt{\gamma_{B,1}} \bar{S}_B^N[\omega] + \sqrt{\gamma_{R,1}} \bar{S}_R^N[\omega] \right] - \bar{S}_B^N[\omega], \quad (\text{A5})$$

where we define the resonator transfer function ($T[\omega]$) as

$$T[\omega_s, \omega] \equiv \frac{\sqrt{\gamma_{B,1}}}{-i(\omega + \omega_s - \omega_1^n) + \frac{\gamma_{\text{tot},1}}{2} - \frac{|g|^2 |a_p|^2}{-i(\omega + \omega_p - \omega_s - \Omega_B) + \frac{\Gamma}{2}}}. \quad (\text{A6})$$

We proceed by computing the power spectral density of the output signal. This yields

$$|S^{\text{out}}[\omega_s, \omega]|^2 = |T[\omega_s, \omega]|^2 \left[\underbrace{\gamma_{A,1} |S^{\text{in}}[\omega_s + \omega]|^2}_{\text{Input Signal}} + \underbrace{\frac{G_B P v_{g,1} \Gamma^2 (n_{\text{th}} + 1/2)}{4((\omega + \omega_p - \omega_s - \Omega_B)^2 + (\frac{\Gamma}{2})^2)}}_{\text{Thermal-mechanical Noise}} + \underbrace{\gamma_{A,1} |\bar{S}_A^N[\omega]|^2 + \left| \sqrt{\gamma_{B,1}} - \frac{1}{T[\omega_s, \omega]} \right|^2 |\bar{S}_B^N[\omega]|^2 + \gamma_{R,1} |\bar{S}_R^N[\omega]|^2}_{\text{Optical Vacuum Fluctuations}} \right], \quad (\text{A7})$$

where the Brillouin gain coefficient G_B is defined as

$$G_B = \frac{4|g|^2 |a_p|^2}{P \Gamma v_{g,1}} \quad (\text{A8})$$

Equation A7 reveals three distinct terms in the output power spectrum; the first term gives the resonant amplification of the input signal, the second arises from thermal-mechanical noise, and the last results from optical vacuum fluctuations. We note here that the cross-terms vanish because the signal and noise sources are uncorrelated (e.g., $\eta^\dagger[\omega] S^{\text{in}}[\omega_s + \omega] = FT[\langle \eta^\dagger(t + \tau) S^{\text{in}}(t) \rangle] = 0$).

We first calculate the signal-wave amplification ($|S^{\text{out}}[\omega_s]|^2 / |S^{\text{in}}[\omega_s]|^2$) by analyzing the spectrum at the center frequency of the input signal (i.e., $\omega = 0$) and ignoring the noise terms, which yields

$$\frac{|S^{\text{out}}[\omega_s]|^2}{|S^{\text{in}}[\omega_s]|^2} = \left| \frac{\sqrt{\gamma_{A,1}} \sqrt{\gamma_{B,1}}}{-i(\omega_s - \omega_1^n) + \frac{\gamma_{\text{tot},1}}{2} - \frac{G_B P v_{g,1} \Gamma/4}{i(\Omega_B + \omega_s - \omega_p) + \Gamma/2}} \right|^2. \quad (\text{A9})$$

This is the central result of this section. We consider the effects of noise in the following section.

2. Noise dynamics

Building on this framework, we can also analyze the quantum-limited noise figure for the amplifier system. The noise figure is defined by

$$\text{NF} = \frac{\text{SNR}_1}{\text{SNR}_2}, \quad (\text{A10})$$

where SNR_1 is the input signal-to-noise ratio (SNR) and SNR_2 is the output signal-to-noise ratio.

As an upper bound on the noise figure, we assume a quantum-limited input signal (i.e., signal relative to the zero-point background; for more details see Ref. [50, 51]). We consider the output SNR over a vanishingly small bandwidth $2\Delta\omega$ ($\Delta\omega \ll \Gamma$) centered around $\omega = 0$. The noise sources are given by the amplified thermal-mechanical and optical vacuum fluctuations (see Eq. A7), while the output signal is given by the amplified input signal. For simplicity, we assume the following functional form for the input signal spectrum: $|S^{\text{in}}[\omega]|^2 = |S^{\text{in}}|^2 \delta(\omega - \omega_s)$, such that

$$\begin{aligned} \text{SNR}_2 &= \frac{\int_{-\Delta\omega}^{\Delta\omega} d\omega \gamma_{A,1} |S^{\text{in}}|^2 \delta(\omega - \omega_s)}{\int_{-\Delta\omega}^{\Delta\omega} d\omega N_b[\omega_s, \omega] + \gamma_{A,1} |\bar{S}_A^N[\omega]|^2 + \left| \sqrt{\gamma_{B,1}} - \frac{1}{T[\omega_s, \omega]} \right|^2 |\bar{S}_B^N[\omega]|^2 + \gamma_{R,1} |\bar{S}_R^N[\omega]|^2} \\ &\simeq \frac{\gamma_{A,1} |S^{\text{in}}|^2}{2\Delta\omega \left[N_b[\omega_s, 0] + \frac{1}{2} \left(\gamma_{A,1} + \left| \sqrt{\gamma_{B,1}} - \frac{1}{T[\omega_s, 0]} \right|^2 + \gamma_{R,1} \right) \right]} \end{aligned} \quad (\text{A11})$$

where $N_b[\omega_s, \omega]$ is defined by

$$N_b[\omega_s, \omega] \equiv \frac{G_B P v_{g,1} \Gamma^2 (n_{th} + 1/2)}{4((\omega + \omega_p - \omega_s - \Omega_B)^2 + (\frac{\Gamma}{2})^2)}. \quad (\text{A12})$$

Here, we have used the correlation properties of the optical vacuum fluctuations to compute each power spectral density (i.e., $|\bar{S}_A^N[\omega]|^2 = \int_{-\infty}^{\infty} d\tau (S_{(A,B,R)}^{N\dagger}(t+\tau) S_{(A,B,R)}^N(t)) e^{i\omega\tau} = \int_{-\infty}^{\infty} d\tau (1/2) \delta(\tau) e^{i\omega\tau} = 1/2$).

We next calculate the input SNR. To calculate an upper bound on the noise figure, we assume a quantum-limited input signal (i.e., limited only by optical vacuum fluctuations). In this case, the input SNR is given by

$$\begin{aligned} \text{SNR}_1 &= \frac{\int_{-\Delta\omega}^{\Delta\omega} d\omega |S^{\text{in}}|^2 \delta(\omega - \omega_s)}{\int_{-\Delta\omega}^{\Delta\omega} d\omega |\bar{S}_A^N[\omega]|^2} \\ &\simeq \frac{|S^{\text{in}}|^2}{\Delta\omega}. \end{aligned} \quad (\text{A13})$$

Now, combining Eq. A11 with Eq. A13, we calculate the noise figure of the system, yielding

$$\begin{aligned} \text{NF} &= \frac{\left[2N_b[\omega_s, 0] + \left(\gamma_{A,1} + \left| \sqrt{\gamma_{B,1}} - \frac{1}{T[\omega_s, 0]} \right|^2 + \gamma_{R,1} \right) \right]}{\gamma_{A,1}} \\ &= \frac{\left[\frac{G_B P v_{g,1} \Gamma^2 (n_{th} + 1/2)}{2((\omega_p - \omega_s - \Omega_B)^2 + (\frac{\Gamma}{2})^2)} + \left(\gamma_{A,1} + \left| \sqrt{\gamma_{B,1}} - \frac{-i(\omega_s - \omega_1^n) + \frac{\gamma_{\text{tot},1}}{2} - \frac{|g|^2 |a_p|^2}{-i(\omega_p - \omega_s - \Omega_B) + \frac{\Gamma}{2}}}{\sqrt{\gamma_{B,1}}} \right|^2 + \gamma_{R,1} \right) \right]}{\gamma_{A,1}} \end{aligned} \quad (\text{A14})$$

We note that the noise figure is signal independent, as it should be [50]. Figure 4a plots the noise figure (Eq. A14) as a function of pump power and detuning from resonance. In the limit of low pump powers or large detunings, Eq. A14 converges to a value that is consistent with the loss produced by linear transmission through the system. When the pump power is increased, additional noise is imparted through spontaneous Brillouin scattering. As the pump power approaches the laser threshold, the quantum-limited noise figure of this silicon Brillouin amplifier system is approximately 38.5 dB relative to the zero-point background. This value is on par with the noise figure of conventional Brillouin amplifiers based on linear waveguides (which can range anywhere between 25 dB to 45 dB depending on the Brillouin frequency). In Brillouin amplifiers (such as the present system), the spontaneous Brillouin emission is narrowly centered around the Brillouin frequency (within ~ 10 MHz), and as such, this system exhibits low out-of-band noise; analyzing the performance of this system over larger bandwidths (~ 300 MHz), for example, yields an effective noise figure that is significantly reduced ($\text{NF} \approx 15$ dB). Moreover, in many practical applications, the input signal typically possesses additional noise—such as relative intensity noise (RIN), amplified spontaneous emission (ASE), or relaxation

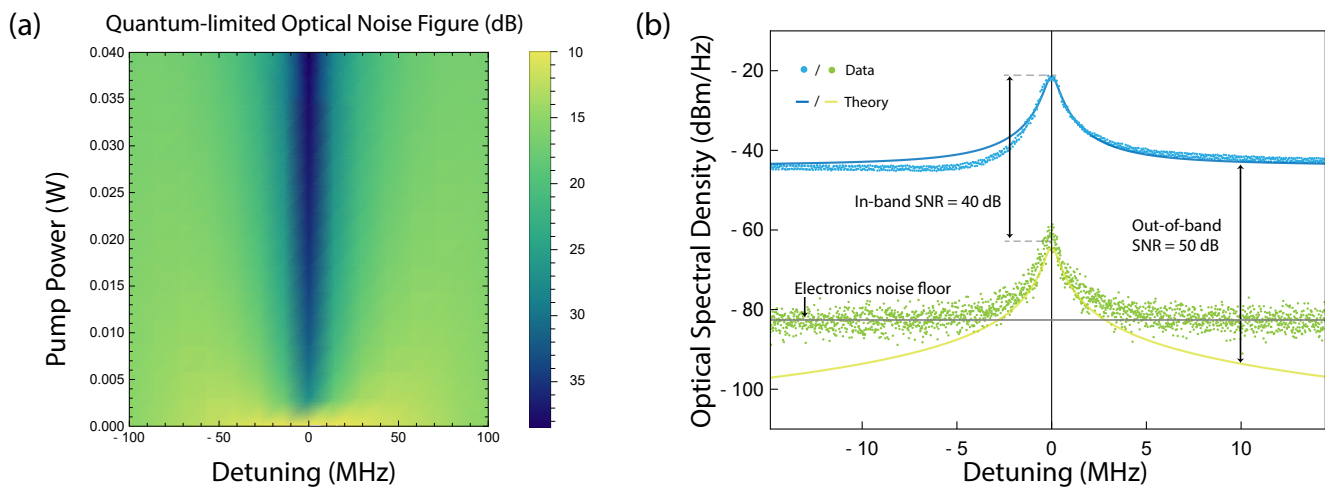


FIG. 4. (a) Theoretical quantum-limited optical noise figure (relative to quantum-limited input signal) as a function of detuning and pump power, obtained from Eq. A14. (b) Output signal (blue), Brillouin noise (light green), and respective theory curves (obtained from Eq. A7, with $P_p = 0.93P_{th}$, where P_{th} is the laser threshold power). Data recorded with RBW = 50 KHz. Theory curves obtained from Eq. A7.

oscillations—whose magnitude far exceeds the zero-point background [52]. Thus, while the quantum-limited noise figure we derive here provides a well-defined upper bound (worst case), the effective noise figure will be more favorable for a large range of practical applications.

a. Experimental measure of noise

We investigate the noise properties of this resonantly enhanced Brillouin amplifier through optical heterodyne laser spectroscopy using the apparatus diagrammed in Fig. 2a of the main text. Figure 4b plots the transmitted signal wave (blue) and the spontaneous optical spectrum (green) versus frequency detuning (relative to the Brillouin frequency Ω_B), demonstrating good agreement with theoretical predictions (see Eq. A7). These results highlight the low out-of-band noise properties of the Brillouin amplifier system.

3. Gain depletion

In this section, we explore the output signal saturation that arises from pump depletion within the resonator. We begin with the mean-field equations of motion under the rotating-wave approximation (Eq. A2). Here, we no longer assume a stiff pump; instead, we adiabatically eliminate the pump dynamics, in accordance with the separation of time scales ($\gamma_p \gg \gamma_s \gg \Gamma$).

In this case, the slowly varying amplitude of the pump wave is given by

$$\bar{a}_p(t) = \frac{2}{\gamma_{\text{tot},2}} \left[-ig\bar{a}_s(t)\bar{b}(t) + \sqrt{\gamma_{A,2}}\bar{S}_p^{\text{in}}(t) \right]. \quad (\text{A15})$$

Next, we substitute Eq. A15 into Eq. A2, ignore thermal and quantum fluctuations, and solve for the steady-state behavior of the system, yielding the following transcendental equation for the signal wave field:

$$\bar{a}_s = \frac{\sqrt{\gamma_{A,1}}\bar{S}_s^{\text{in}}}{\left[-i(\omega_s - \omega_1^n) + \frac{\gamma_{\text{tot},1}}{2} + \frac{G_B^2 \hbar \omega_p P v_{g,1}^2 v_{g,2} \Gamma^2 / (8\gamma_{\text{tot},2} L)}{(\omega_p - \omega_s - \Omega_B)^2 + (\Gamma/2 + G_B \hbar \omega_p v_{g,1} v_{g,2} \Gamma |\bar{a}_s|^2 / (2\gamma_{\text{tot},2} L))^2} - \frac{G_B P v_{g,1} \Gamma / 4}{i(\omega_p - \omega_s - \Omega_B) + \Gamma/2 + G_B \hbar \omega_p v_{g,1} v_{g,2} \Gamma |\bar{a}_s|^2 / (2\gamma_{\text{tot},2} L)} \right]}. \quad (\text{A16})$$

As this equation becomes analytically intractable, we proceed by solving Eq. A16 numerically.

We also explore this gain depletion behavior through a set of systematic experimental studies. This approach involves analyzing the transmitted signal-wave spectrum versus frequency over a range of input signal-wave powers; data from these measurements are presented in Fig. 5. Through these measurements, we observe a clear reduction in the gain as we increase the input signal wave power, in good agreement with our pump-depletion-based theoretical predictions.

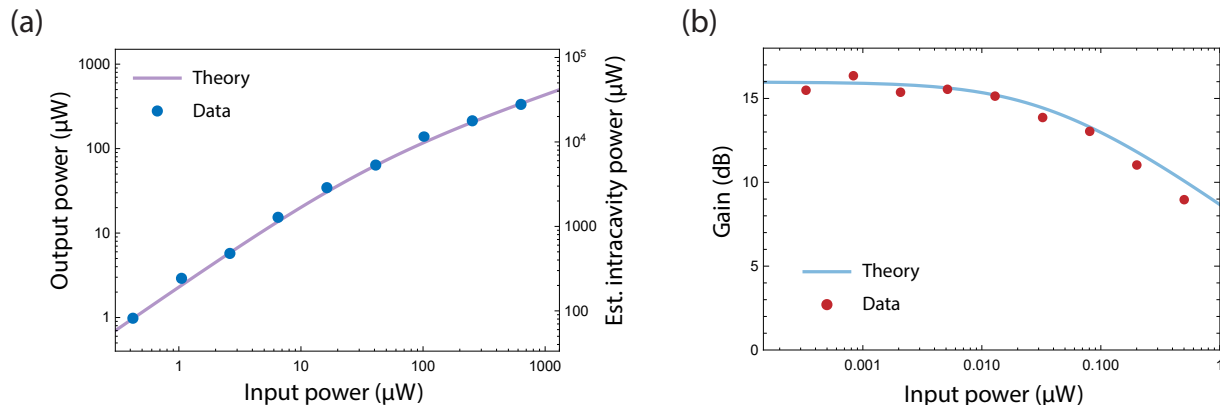


FIG. 5. (a) Output signal wave power as a function of input signal wave power. (b) Gain versus input power. Theoretical curves are obtained by numerically solving Eq. A16 (with $P = 0.86P_{\text{th}}$, $\mu_{A,1}^2 = 0.16$, and $\mu_{B,1}^2 = 0.012$)

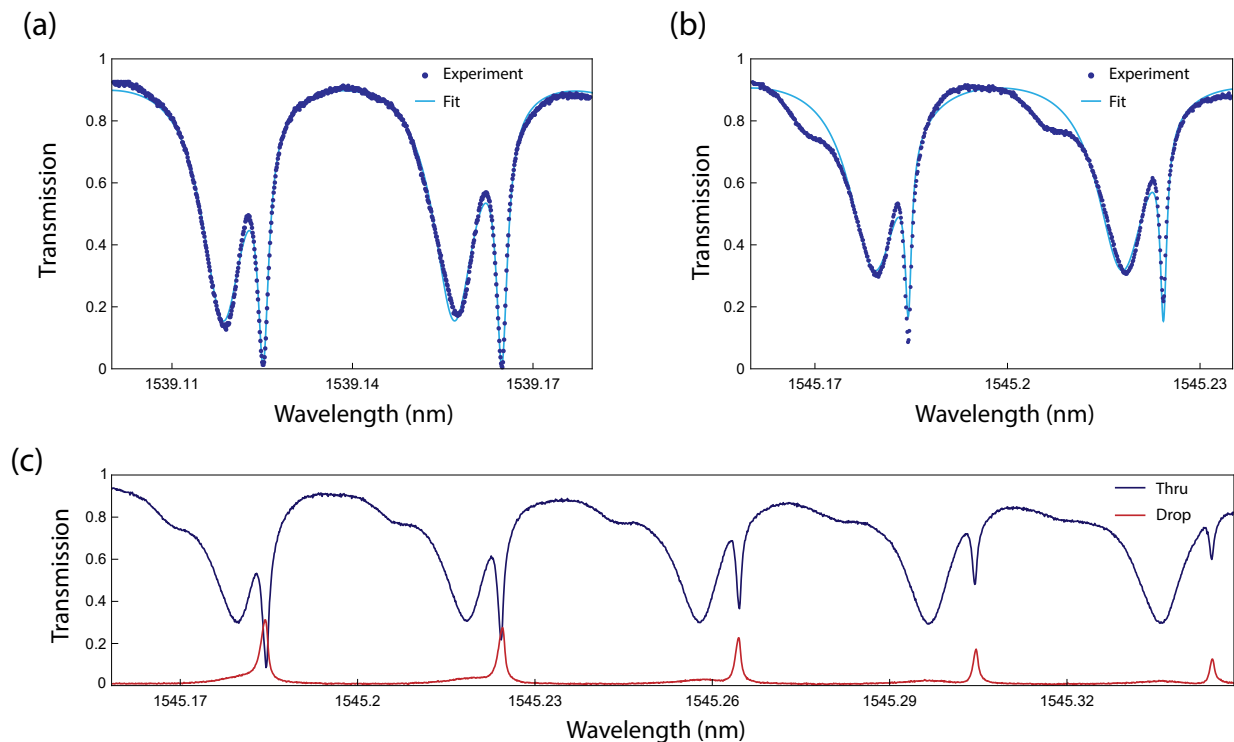


FIG. 6. (a)-(b) Linear (thru) transmission spectra centered around two distinct mode pairs that satisfy the Brillouin condition ($\omega_1^n = \omega_2^m - \Omega_B$). Narrow (broad) resonances correspond to the symmetric (antisymmetric) spatial modes of the multimode waveguide. Fits are obtained using the multimode ring resonator theory presented in the Supplementary Materials of Ref. [21]. (c) Transmission spectra measured at the thru and drop ports over a larger wavelength range.

Appendix B: Passive resonator properties

In this section, we present a brief explanation of the passive resonator properties. The multi-spatial mode racetrack cavity produces two distinct sets of cavity modes, yielding a characteristic multimode transmission spectrum (see Fig. 6c). We measure the linear transmission response of the cavity using a swept 1.55 μm laser (Agilent 81600B; sweep rate set to 5 nm/s) at low powers ($\sim 120 \mu\text{W}$ on-chip). Fig. 6a-b plots the measured transmission (thru) spectra centered around two distinct mode pairs that satisfy the Brillouin condition ($\omega_1^n = \omega_2^m - \Omega_B$), while Fig. 6c shows the transmission spectra measured at the thru and drop ports over a larger wavelength range. Fitting these transmission spectra to a multimode resonator model (see Supplementary Materials of Ref. [21]) allows us to obtain important parameters of the system, including the multimode coupling coefficients, group velocities, and linear propagation losses (see Table I). This information is then used to model the amplifier dynamics (for example, see theory curve in Fig. 2d-e of the main text).

Appendix C: Experimental considerations and data analysis

1. Nonreciprocal amplification characterization

An important feature of this Brillouin system is that the amplification process is inherently nonreciprocal. This property arises from the time modulation induced and sustained by the coherent phonon field. Alternatively, this phenomena can also be understood through the energy and phase-matching conditions required by this traveling-wave process (see Fig. 7b-c). The phonon field that mediates the Brillouin amplification cannot mediate coupling in the backward direction as a result of phase-matching. Moreover, the phonon frequency and wavevector that would be required for a backward process (between counter-propagating waves) is not supported by the acoustic dispersion relation. These phase-matching and energy-conservation considerations are illustrated succinctly by the diagrams presented in Fig. 7b-c.

We next detail the experimental approach and apparatus used to investigate the nonreciprocal nature of this resonantly enhanced Brillouin amplifier (data presented in Fig. 3c of the main text). As diagrammed in Fig. 7a, these measurements involve the use of a fiber-optic switch, which allows us to rapidly change the propagation direction of the signal wave relative to the pump wave. Throughout the experiments, the pump wave is coupled into a counter-clockwise anti-symmetric mode of the resonator that is separated from a symmetric cavity mode by the Brillouin frequency ($\omega_p = \omega_2^m$,

$\omega_2^m - \omega_1^n = \Omega_B$). We then measure the signal wave transmission in the forward and backward directions as we sweep the signal-wave frequency $\omega_s = \omega_p - \Omega$ through the dual resonance condition ($\omega_s = \omega_1^n = \omega_p - \Omega_B$).

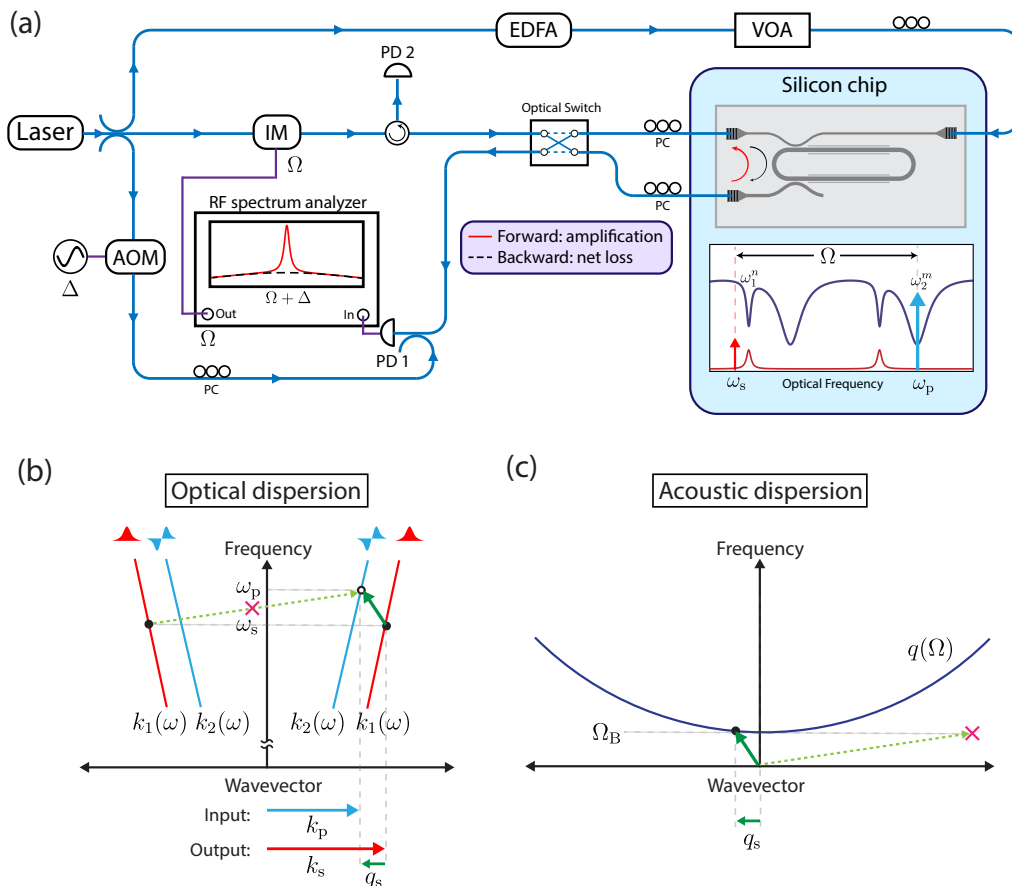


FIG. 7. Nonreciprocal optical amplification measurements. (a) Diagram of the experimental apparatus used to characterize the nonreciprocal nature of the resonantly enhanced Brillouin amplifier. Laser light is split along three paths. The first (top) is used to generate a pump wave of a desired optical power, which is subsequently coupled on-chip. The second arm synthesizes the signal wave with the desired frequency detuning ($\Omega = \omega_p - \omega_s$) using an intensity modulator (IM). Finally, the third creates an optical local oscillator (LO) using an acousto-optic modulator (AOM), which blueshifts the light by $\Delta = 44$ MHz. An optical switch directs the signal wave light on-chip such that it either co- or counter-propagates with the pump wave within the resonator. After passing through the device, the signal wave is coupled through the drop port and off-chip, where it is combined with the blueshifted LO and measured on a high-speed photodetector (PD 1). (b)-(c) diagrams illustrating energy and phase-matching conditions imposed by the optical and acoustic dispersion relations. In this diagram, the dark green arrow represents the frequency and wavevector of the phonon that mediates stimulated inter-modal Brillouin scattering, while the dotted light-green arrow shows the phonon that would be required to mediate amplification in the backward direction, which is not supported by the acoustic dispersion relation. Thus, the elastic wave that mediates forward stimulated inter-modal Brillouin scattering does not mediate a backward scattering process.

2. System parameters and data analysis

In this section, we detail the experimental parameters of the system and how they are determined. All parameters in the system are corroborated by a self-consistent model of the amplifier dynamics. We enumerate these parameters in Table I. The passive optical properties of the resonator system are obtained by fitting the transmission spectrum to a multi-spatial mode resonator model (for more details, see section B of this Appendix and Supplementary Materials of Ref. [21]). As the couplers A and B are wavelength dependent, we indicate an approximate range for each coupling coefficient. The acoustic dissipation rate is determined by analyzing the Brillouin-gain bandwidths at low intracavity pump powers. The Brillouin-gain coefficient is extracted by fitting the mean-field model to our measurements (see Fig. 2c of the main text). Altogether, these parameters are in agreement with those previously obtained in similar device geometries [21].

To determine the degree of net amplification (for Fig. 2 of the main text), we calibrate the signal-wave transmission through the resonant system by comparing it to the signal-wave transmission through a linear device on the same chip (placed $600 \mu\text{m}$ away). Data for Fig. 2c-d of the main text were obtained by acquiring traces as the signal-wave detuning

Optical properties	Description	Value
L	Length of device	1.57 cm
W_m	Acoustic membrane width	2.85 μm
W_o	Optical waveguide width	1.5 μm
FSR ₁	Free spectral range of symmetric mode	5.02 GHz
FSR ₂	Free spectral range of antisymmetric mode	4.87 GHz
$\mu_{A,1}^2$	Coupling through coupler A into the symmetric mode	0.045-0.16
$\mu_{A,2}^2$	Coupling through coupler A into the antisymmetric mode	0.62-0.71
$\mu_{B,1}^2$	Coupling through coupler B into the symmetric mode	0.01-0.07
$\mu_{B,2}^2$	Coupling through coupler B into the antisymmetric mode	0.007-0.016
α_1	Symmetric spatial mode propagation loss	6.7 m^{-1}
α_2	Antisymmetric spatial mode propagation loss	20.6 m^{-1}
$v_{g,2}$	Symmetric spatial mode group velocity	7.91×10^7 m/s
$v_{g,1}$	Antisymmetric spatial mode group velocity	7.67×10^7 m/s
Ω_B	Brillouin frequency	2π 5.95 GHz
Γ	Acoustic dissipation rate	2π 9 MHz
G_B	Brillouin gain coefficient	380 $\text{W}^{-1}\text{m}^{-1}$

TABLE I. Experimental parameters of the nonreciprocal resonantly enhanced silicon Brillouin amplifier

(Ω) is swept through the Brillouin frequency (Ω_B) while sweeping the the pump power and varying pump wavelength around the dual-resonance condition (i.e., $\omega_p = \omega_2^m$, $\omega_p - \Omega_B = \omega_1^n$). The data in Fig. 2c-d represent the traces obtained with near-zero detuning ($\omega_p - \Omega_B - \omega_1^n$). Intracavity powers are estimated using the passive ring resonator parameters and accounting for the effects of nonlinear loss; additionally, this analysis is consistent with the power-dependent nature of the directional couplers.

3. Device fabrication

The Brillouin amplifier devices are fabricated on a single-crystal silicon-on-insulator chip (215 nm silicon, 3 μm SiO₂) using a two-step electron-beam lithography process (for additional details, see [19–21]). Optical waveguides are defined through electron-beam lithography (using hydrogen silsesquioxane (HSQ) electron-beam resist), followed by development in MF-312 and an anisotropic Cl₂ reactive ion etch (RIE), which removes 80 nm of silicon. A subsequent lithography step is used to pattern slots with CSAR electron-beam resist. After development in Xylenes, the remainder of the silicon is removed through another RIE etch, exposing the oxide underneath the slotted regions. Finally, a wet-etch (49% hydrofluoric acid) is used to remove the oxide undercladding to create a continuously suspended Brillouin-active waveguide. The phonon membrane dimensions are 2.85 $\mu\text{m} \times 135$ nm, while the multimode optical ridge waveguide is 1.5 $\mu\text{m} \times 215$ nm [20, 21].

-
- [1] Juerg Leuthold, C Koos, and W Freude, “Nonlinear silicon photonics,” *Nat. Photonics* **4**, 535 (2010).
- [2] Di Liang and John E Bowers, “Recent progress in lasers on silicon,” *Nat. Photonics* **4**, 511 (2010).
- [3] Hyundai Park, Alexander W Fang, Oded Cohen, Richard Jones, Mario J Paniccia, and John E Bowers, “A hybrid AlGaInAs-silicon evanescent amplifier,” *IEEE Photonics Technology Letters* **19**, 230–232 (2007).
- [4] Martijn JR Heck, Hui-Wen Chen, Alexander W Fang, Brian R Koch, Di Liang, Hyundai Park, Matthew N Sysak, and John E Bowers, “Hybrid silicon photonics for optical interconnects,” *IEEE J. Sel. Top. Quantum Electron.* **17**, 333–346 (2011).
- [5] Shahram Keyvaninia, Günther Roelkens, Dries Van Thourhout, M Lamponi, F Lelarge, J-M Fedeli, S Messaoudene, EJ Geluk, B Smalbrugge, *et al.*, “A highly efficient electrically pumped optical amplifier integrated on a SOI waveguide circuit,” in *Group IV Photonics (GFP), 2012 IEEE 9th International Conference on* (IEEE, 2012) pp. 222–224.
- [6] Laura Agazzi, Jonathan DB Bradley, Meindert Dijkstra, Feridun Ay, Gunther Roelkens, Roel Baets, Kerstin Wörhoff, and Markus Pollnau, “Monolithic integration of erbium-doped amplifiers with silicon-on-insulator waveguides,” *Opt. Express* **18**, 27703–27711 (2010).
- [7] Ricardo Claps, Dimitri Dimitropoulos, Varun Raghunathan, Y Han, and B Jalali, “Observation of stimulated Raman amplification in silicon waveguides,” *Opt. Express* **11**, 1731–1739 (2003).
- [8] Ozdal Boyraz and Bahram Jalali, “Demonstration of 11 dB fiber-to-fiber gain in a silicon Raman amplifier,” *IEICE Electron. Expr.* **1**, 429–434 (2004).
- [9] TK Liang and HK Tsang, “Efficient Raman amplification in silicon-on-insulator waveguides,” *Appl. Phys. Lett.* **85**, 3343–3345 (2004).
- [10] Ansheng Liu, Haisheng Rong, Mario Paniccia, Oded Cohen, and Dani Hak, “Net optical gain in a low loss silicon-on-insulator waveguide by stimulated Raman scattering,” *Opt. Express* **12**, 4261–4268 (2004).
- [11] Mark A Foster, Amy C Turner, Jay E Sharping, Bradley S Schmidt, Michal Lipson, and Alexander L Gaeta, “Broadband optical parametric gain on a silicon photonic chip,” *Nature* **441**, 960 (2006).

- [12] Xiaoping Liu, Richard M Osgood Jr, Yurii A Vlasov, and William MJ Green, “Mid-infrared optical parametric amplifier using silicon nanophotonic waveguides,” *Nature Photonics* **4**, 557 (2010).
- [13] Bart Kuyken, Xiaoping Liu, Günther Roelkens, Roel Baets, Richard M Osgood Jr, and William MJ Green, “50 dB parametric on-chip gain in silicon photonic wires,” *Opt. Lett.* **36**, 4401–4403 (2011).
- [14] Haisheng Rong, Richard Jones, Ansheng Liu, Oded Cohen, Dani Hak, Alexander Fang, and Mario Paniccia, “A continuous-wave Raman silicon laser,” *Nature* **433**, 725 (2005).
- [15] Peter T Rakich, Charles Reinke, Ryan Camacho, Paul Davids, and Zheng Wang, “Giant enhancement of stimulated Brillouin scattering in the subwavelength limit,” *Phys. Rev. X* **2**, 011008 (2012).
- [16] Heedeuk Shin, Wenjun Qiu, Robert Jarecki, Jonathan A Cox, Roy H Olsson III, Andrew Starbuck, Zheng Wang, and Peter T Rakich, “Tailorable stimulated Brillouin scattering in nanoscale silicon waveguides,” *Nat. Commun.* **4**, 1944 (2013).
- [17] Raphaël Van Laer, Bart Kuyken, Dries Van Thourhout, and Roel Baets, “Interaction between light and highly confined hypersound in a silicon photonic nanowire,” *Nat. Photonics* **9**, 199 (2015).
- [18] Raphaël Van Laer, Alexandre Bazin, Bart Kuyken, Roel Baets, and Dries Van Thourhout, “Net on-chip Brillouin gain based on suspended silicon nanowires,” *New J. Phys.* **17**, 115005 (2015).
- [19] Eric A Kittlaus, Heedeuk Shin, and Peter T Rakich, “Large Brillouin amplification in silicon,” *Nat. Photonics* **10**, 463 (2016).
- [20] Eric A Kittlaus, Nils T Otterstrom, and Peter T Rakich, “On-chip inter-modal Brillouin scattering,” *Nat. Commun.* **8**, 15819 (2017).
- [21] Nils T Otterstrom, Ryan O Behunin, Eric A Kittlaus, Zheng Wang, and Peter T Rakich, “A silicon Brillouin laser,” *Science* **360**, 1113–1116 (2018).
- [22] Takuo Tanemura, Yuichi Takushima, and Kazuro Kikuchi, “Narrowband optical filter, with a variable transmission spectrum, using stimulated Brillouin scattering in optical fiber,” *Opt. Lett.* **27**, 1552–1554 (2002).
- [23] Ravi Pant, David Marpaung, Irina V Kabakova, Blair Morrison, Christopher G Poulton, and Benjamin J Eggleton, “On-chip stimulated Brillouin scattering for microwave signal processing and generation,” *Laser Photonics Rev.* **8**, 653–666 (2014).
- [24] Yahia Souidi, Fethallah Taleb, Junbo Zheng, Min Won Lee, Frédéric Du Burck, and Vincent Roncin, “Low-noise and high-gain Brillouin optical amplifier for narrowband active optical filtering based on a pump-to-signal optoelectronic tracking,” *Appl. Opt.* **55**, 248–253 (2016).
- [25] Amol Choudhary, Blair Morrison, Iman Aryanfar, Shayan Shahnia, Mattia Pagani, Yang Liu, Khu Vu, Stephen Madden, David Marpaung, and Benjamin J Eggleton, “Advanced integrated microwave signal processing with giant on-chip Brillouin gain,” *J. Lightwave Technol.* **35**, 846–854 (2017).
- [26] Kozlovskii, “Detection of weak optical signals with a laser amplifier,” *J. Exp. Theor. Phys.* **102**, 24–33 (2006).
- [27] Christian Wolff, Philipp Gutsche, Michael J Steel, Benjamin J Eggleton, and Christopher G Poulton, “Power limits and a figure of merit for stimulated Brillouin scattering in the presence of third and fifth order loss,” *Opt. Express* **23**, 26628–26638 (2015).
- [28] Myeong Soo Kang, A Butsch, and P St J Russell, “Reconfigurable light-driven opto-acoustic isolators in photonic crystal fibre,” *Nat. Photonics* **5**, 549 (2011).
- [29] Christopher G Poulton, Ravi Pant, Adam Byrnes, Shanhui Fan, MJ Steel, and Benjamin J Eggleton, “Design for broadband on-chip isolator using stimulated Brillouin scattering in dispersion-engineered chalcogenide waveguides,” *Opt. Express* **20**, 21235–21246 (2012).
- [30] Amir H Safavi-Naeini, TP Mayer Alegre, Jasper Chan, Matt Eichenfield, Martin Winger, Qiang Lin, Jeff T Hill, Darrick E Chang, and Oskar Painter, “Electromagnetically induced transparency and slow light with optomechanics,” *Nature* **472**, 69 (2011).
- [31] Elias Giacomidis, Amol Choudhary, Eric Magi, David Marpaung, Khu Vu, Pan Ma, Duk-Yong Choi, Steve Madden, Bill Corcoran, Mark Pelusi, *et al.*, “Chip-based Brillouin processing for carrier recovery in self-coherent optical communications,” *Optica* **5**, 1191–1199 (2018).
- [32] Kwang Yong Song, Miguel González Herráez, and Luc Thévenaz, “Observation of pulse delaying and advancement in optical fibers using stimulated Brillouin scattering,” *Opt. Express* **13**, 82–88 (2005).
- [33] Yoshitomo Okawachi, Matthew S Bigelow, Jay E Sharping, Zhaoming Zhu, Aaron Schweinsberg, Daniel J Gauthier, Robert W Boyd, and Alexander L Gaeta, “Tunable all-optical delays via Brillouin slow light in an optical fiber,” *Phys. Rev. Lett.* **94**, 153902 (2005).
- [34] Ravi Pant, Adam Byrnes, Christopher G Poulton, Enbang Li, Duk-Yong Choi, Steve Madden, Barry Luther-Davies, and Benjamin J Eggleton, “Photonic-chip-based tunable slow and fast light via stimulated Brillouin scattering,” *Opt. Lett.* **37**, 969–971 (2012).
- [35] Dimitrios L Sounas and Andrea Alù, “Non-reciprocal photonics based on time modulation,” *Nat. Photonics* **11**, 774 (2017).
- [36] Mohammad-Ali Miri, Freek Ruesink, Ewold Verhagen, and Andrea Alù, “Optical nonreciprocity based on optomechanical coupling,” *Phys. Rev. Appl.* **7**, 064014 (2017).
- [37] JunHwan Kim, Mark C Kuzyk, Kewen Han, Hailin Wang, and Gaurav Bahl, “Non-reciprocal Brillouin scattering induced transparency,” *Nat. Phys.* **11**, 275 (2015).
- [38] Chun-Hua Dong, Zhen Shen, Chang-Ling Zou, Yan-Lei Zhang, Wei Fu, and Guang-Can Guo, “Brillouin-scattering-induced transparency and non-reciprocal light storage,” *Nat. Commun.* **6**, 6193 (2015).
- [39] Zhen Shen, Yan-Lei Zhang, Yuan Chen, Chang-Ling Zou, Yun-Feng Xiao, Xu-Bo Zou, Fang-Wen Sun, Guang-Can Guo, and Chun-Hua Dong, “Experimental realization of optomechanically induced non-reciprocity,” *Nat. Photonics* **10**, 657 (2016).
- [40] Freek Ruesink, Mohammad-Ali Miri, Andrea Alu, and Ewold Verhagen, “Nonreciprocity and magnetic-free isolation based on optomechanical interactions,” *Nat. Commun.* **7**, 13662 (2016).
- [41] Shiyue Hua, Jianming Wen, Xiaoshun Jiang, Qian Hua, Liang Jiang, and Min Xiao, “Demonstration of a chip-based optical isolator with parametric amplification,” *Nat. Commun.* **7**, 13657 (2016).
- [42] Kejie Fang, Jie Luo, Anja Metelmann, Matthew H Matheny, Florian Marquardt, Aashish A Clerk, and Oskar Painter, “Generalized non-reciprocity in an optomechanical circuit via synthetic magnetism and reservoir engineering,” *Nat. Phys.* **13**, 465 (2017).
- [43] Yuya Shoji, Tetsuya Mizumoto, Hideki Yokoi, I-Wei Hsieh, and Richard M Osgood Jr, “Magneto-optical isolator with silicon waveguides fabricated by direct bonding,” *Appl. Phys. Lett.* **92**, 071117 (2008).
- [44] Lei Bi, Juejun Hu, Peng Jiang, Dong Hun Kim, Gerald F Dionne, Lionel C Kimerling, and CA Ross, “On-chip optical isolation in monolithically integrated non-reciprocal

- optical resonators,” *Nat. Photonics* **5**, 758 (2011).
- [45] Duanni Huang, Paolo Pintus, Chong Zhang, Yuya Shoji, Tetsuya Mizumoto, and John E Bowers, “Electrically driven and thermally tunable integrated optical isolators for silicon photonics,” *IEEE J. Sel. Top. Quantum Electron.* **22**, 4403408 (2016).
- [46] Paolo Pintus, Duanni Huang, Paul Adrian Morton, Yuya Shoji, Tetsuya Mizumoto, and John E Bowers, “Broadband te optical isolators and circulators in silicon photonics through ce: Yig bonding,” *J. Lightwave Technol.* (2019).
- [47] Donggyu B Sohn, Seunghwi Kim, and Gaurav Bahl, “Time-reversal symmetry breaking with acoustic pumping of nanophotonic circuits,” *Nat. Photonics* **12**, 91 (2018).
- [48] Eric A Kittlaus, Nils T Otterstrom, Prashanta Kharel, Shai Gertler, and Peter T Rakich, “Non-reciprocal interband Brillouin modulation,” *Nat. Photonics* **12**, 613 (2018).
- [49] Brent E Little, Sai T Chu, Hermann A Haus, J Foresi, and J-P Laine, “Microring resonator channel dropping filters,” *J. Lightwave Technol.* **15**, 998–1005 (1997).
- [50] HA Haus, “The noise figure of optical amplifiers,” *IEEE Photonic Tech L.* **10**, 1602–1604 (1998).
- [51] Bruno Bristiel, Shifeng Jiang, Philippe Gallion, and Erwan Pincemin, “New model of noise figure and rin transfer in fiber Raman amplifiers,” *IEEE Photonic Tech L.* **18**, 980–982 (2006).
- [52] Vincent Jude Urick, Keith J Williams, and Jason D McKinney, *Fundamentals of microwave photonics*, Vol. 1 (John Wiley & Sons, 2015).